Phys Chem Minerals (2018) 45:353–359
DOI 10.1007/s00269-017-0925-y

ORIGINAL PAPER

Pressure-dependent Raman spectra of $Ba_5(PO_4)_3Cl$ alforsite

Shuangmeng Zhai[1] · Zeming Li[1,2] · Sean R. Shieh[3] · Ching-Pao Wang[3] · Weihong Xue[1]

Received: 11 May 2017 / Accepted: 11 October 2017 / Published online: 16 October 2017

Abstract The pressure-dependent Raman spectra of synthetic alforsite, $Ba_5(PO_4)_3Cl$, were investigated up to 34.9 GPa using a DAC at room temperature. During compression to greater than 20 GPa, new Raman active peaks of $Ba_5(PO_4)_3Cl$ were observed. The Raman frequencies of all observed bands for $Ba_5(PO_4)_3Cl$ alforsite increase continuously with increasing pressure. The quantitative analysis of PO_4 internal vibrational pressure dependences for different Raman bands in alforsite shows that the ν_3 anti-symmetric stretching modes have larger pressure coefficients (from 4.24 to 5.46 cm^{-1}/GPa) whereas, the ν_4 anti-symmetric bending vibrations have smaller pressure coefficients (from 1.16 to 2.04 cm^{-1}/GPa). The external modes show larger pressure coefficients (from 4.71 to 5.54 cm^{-1}/GPa). The PO_4 internal modes in $Ba_5(PO_4)_3Cl$ alforsite give isothermal mode Grüneisen parameters varying from 0.147 to 0.488, which yields an average PO_4 internal mode Grüneisen parameter of 0.314. On the other hand, the external modes give isothermal mode Grüneisen parameters from 1.583 to 2.030. The external modes mainly contribute to the bulk Grüneisen parameter since the bulk thermochemical Grüneisen parameter was determined as 1.44.

✉ Shuangmeng Zhai
zhaishuangmeng@vip.gyig.ac.cn

[1] Key Laboratory of High-temperature and High-pressure Study of the Earth's Interior, Institute of Geochemistry, Chinese Academy of Sciences, Guiyang 550081, Guizhou, China

[2] University of Chinese Academy of Sciences, Beijing 100049, China

[3] Department of Earth Sciences, University of Western Ontario, London, ON N6A 5B7, Canada

Keywords Alforsite · $Ba_5(PO_4)_3Cl$ · Raman spectra · High pressure

Introduction

Apatite, $Ca_5(PO_4)_3X$ (X = F, Cl, OH), is an abundant and common phosphate phase and an important accessory mineral, that widely exists in sedimentary, igneous and metamorphic rocks with various implications for mineralogy and geochemistry. Due to its unique structure and chemistry, apatite can accommodate numerous cations substitutions for Ca^{2+} (Hughes and Rakovan 2002; Pan and Fleet 2002), yielding many apatite-group minerals (Huminicki and Hawthorne 2002; White et al. 2005; Pasero et al. 2010; Hughes and Rakovan 2015). Alforsite is one of apatite-group minerals with chemical formula of $Ba_5(PO_4)_3Cl$, which was first discovered in contact metamorphosed evaporitic rocks associated with fluorapatite and many other rare barium minerals, as reported by Newberry et al. (1981). In fact, alforsite $Ba_5(PO_4)_3Cl$ containing rare earth element dopants is widely studied as fluorescent and laser materials (Yu et al. 1988; Sato et al. 1994; Noginov et al. 2000; Yoo et al. 2009; Ju et al. 2013; Kim et al. 2016). The crystal structure of $Ba_5(PO_4)_3Cl$ was determined by Hata et al. (1979) and is represented in Fig. 1. Similar to fluorapatite, alforsite has a hexagonal structure with space group of $P6_3/m$, in which two kinds of Ba^{2+} cations are Ba1 located on a threefold axis with nine coordinate and Ba2 in distorted pentagonal bipyramidal geometry with one bond to Cl and six bonds with O neighbors. The phosphorous is in tetrahedrally coordinated geometry with a central P atom.

The abundance of apatite in the lithospheric mantle may be greatly underestimated (O'Reilly and Griffin 2000). The physical properties of apatite-group minerals under high

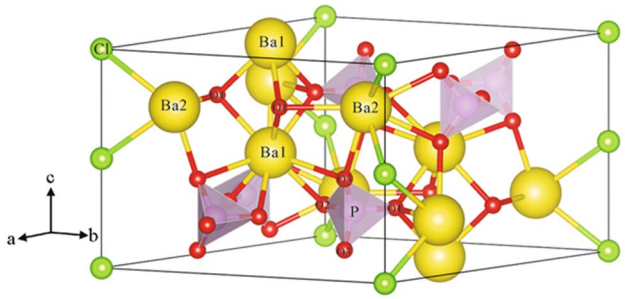

Fig. 1 Crystal structure of alforsite, the image was obtained using VESTA (Momma and Izumi 2011)

pressures are fundamental for mineralogy since apatites can exist in the deep mantle through subduction. Previous high-pressure studies of apatite-group minerals mostly focused on fluorapatite, hydroxylapatite and chlorapatite (Allan et al. 1996; Williams and Knittle 1996; Brunet et al. 1999; Comodi et al. 2001a, b; Matsukage et al. 2004; Fan et al. 2013a, b). Some studies on lead fluoapatite (Liu et al. 2008; Fleet et al. 2010; He et al. 2012), vanadinite (Gatta et al. 2009; Fan et al. 2013a, b), lead bromapatite (Liu et al. 2011a), carbonated hydroxylapatite (Liu et al. 2011b; Forien et al. 2015), mimetite (Wei et al. 2013), pyromorphite (Wei et al. 2013), stronadelphite (He et al. 2013; Zhai et al. 2015a) under high pressures were reported. It's noted that most of these studies concentrate on the compressibility. Only three studies reported the high-pressure Raman spectra of fluorapatite (Williams and Knittle 1996; Comodi et al. 2001a) and stronadelphite (Zhai et al. 2015a). More pressure-dependent vibrational investigations of apatite-group minerals are strongly needed in order to better understand their physical properties under high pressures.

In this paper we report the first high-pressure micro-Raman spectroscopic study on $Ba_5(PO_4)_3Cl$ up to 34.9 GPa at room temperature using a diamond-anvil cell. The study has been performed over the frequency range from 150 to 1200 cm^{-1}. The effect of pressure on the characteristic Raman active modes of alforsite is analyzed. Combined with previous results of isothermal bulk moduli for synthetic and natural hexagonal apatites, the isothermal mode Grüneisen parameters of alforsite are calculated and compared with other phosphate minerals including fluorapatite, tuite, whitlockite, stronadelphite.

Experimental

High-purity alforsite $Ba_5(PO_4)_3Cl$ was prepared by solid-state reactions from $NH_4H_2PO_4$, $BaCO_3$ and $BaCl_2$. Reagent-grade $NH_4H_2PO_4$, $BaCO_3$ and $BaCl_2$ powders were mixed in the proportion corresponding to the $Ba_5(PO_4)_3Cl$ stoichiometry, and the mixture was ground for 2 h in an agate mortar and pressed into pellets with a diameter of 5 mm under a uniaxial pressure of 30 MPa. The pellets were first sintered at 1273 K for 36 h, and then ground and calcined at 1273 K for 36 h again, to form a single phase. The synthesized product was ground finely and characterized by powder X-ray diffraction. The X-ray diffraction pattern confirmed the synthetic product is a single $Ba_5(PO_4)_3Cl$ phase. The refinement yields unit cell parameters as $a = 10.2627(11)$ Å, $c = 7.6511(12)$ Å, and $V = 697.9(1)$ $Å^3$, which are consistent with previous studies (Hata et al. 1979; Newberry et al. 1981; Babu et al. 2011).

By using a symmetric type of diamond-anvil cell (DAC) with a pair of 300 μm culet diamond anvils, the high-pressure Raman spectra of $Ba_5(PO_4)_3Cl$ were collected at room temperature. The experimental method used in this study was same as previous study (Zhai et al. 2015a). A stainless steel plate with an initial thickness of 250 μm was used as gasket. The central area of the gasket was pre-indented to a thickness of about 30 μm, and a hole of 100 μm in diameter was drilled at the center to serve as sample chamber. The synthetic sample and ruby (Cr^{3+} doped α-Al_2O_3) spheres (for pressure calibration), were loaded into the sample chamber. Ar was used as the pressure medium. The experimental pressures were determined by the ruby fluorescence method (Mao et al. 1978). Micro-Raman spectra were collected in backscattering geometry by a custom-built Raman system with a liquid nitrogen cooled CCD detector, 20× objective, at University of Western Ontario. The spectrometer focal length is 500 mm and the grating is 1800 g/mm. An argon-ion laser with a wavelength of 514.5 nm was used as exciting source and a spectrometer with a liquid nitrogen cooled CCD detector was used to collect the Raman data. The spectrometer was calibrated by a neon lamp and the precision of the frequency was about 1 cm^{-1}. The data collection time was 120 s for each spectrum. The spectrometer position was moved to 529 nm to collect external and bending modes (ν_2 and ν_4), and to 538 nm for the stretching modes (ν_1 and ν_3). The Raman shift of each band was obtained by Lorentzian curve fitting using the PeakFit program (SPSS Inc., Chicago).

Results and discussion

Raman spectrum at ambient conditions

An isolated PO_4 tetrahedron has T_d symmetry and four normal internal modes of vibration: $\nu_1(A_1)$ symmetric stretching vibrations of the P–O bond (938 cm^{-1}), $\nu_2(E)$ symmetric bending vibrations of the O–P–O angle (420 cm^{-1}), $\nu_3(T_2)$ anti-symmetric stretching vibrations of the P–O bond (1017 cm^{-1}) and $\nu_4(T_2)$ anti-symmetric bending vibrations

of the O–P–O angle (567 cm^{-1}), where the species E vibrations are doubly degenerate and T_2 vibrations are triply degenerate (Griffith 1969). The effect of the crystal field in the alforsite lattice on the internal modes may be understood by considering the phosphate site symmetry. The T_d symmetry of a free PO_4 tetrahedron is reduced to Cs in the crystal lattice. This symmetry change reduces some of the degeneracies of the vibrational wave functions which would have characterized free PO_4 tetrahedra. According to the factor group analysis (Klee 1970) based on the $P6_3/m$ space group (C_{6h}^2) of fluorapatite, the isostructural $Ba_5(PO_4)_3Cl$ yields the following Raman active vibrations:

$$\Gamma = 12A_g + 8E_{1g} + 13E_{2g}.$$

Therefore, a total of 33 Raman vibrational modes are predicted. Among these, the phosphate tetrahedron shares the following internal and external modes (Toumi et al. 2000):

$$\Gamma\left(PO_4\,\text{internal}\right) = 6A_g + 3E_{1g} + 6E_{2g}.$$

$$\Gamma\left(PO_4\text{external}\right) = 3A_g + 3E_{1g} + 3E_{2g}.$$

As illustrated in Fig. 2, the Raman spectrum of alforsite at ambient conditions shows 13 peaks, which is less than the predicted number due to overlapping or/and the weak intensity of some peaks. The band originating from the ν_2 symmetric bending vibrations splits into two bands at 411 and 426 cm^{-1}, the band connected with the ν_4 anti-symmetric bending vibrations splits into three bands at 563, 570 and 585 cm^{-1}, the bands at 982, 1004, 1016, 1028 and 1046 cm^{-1} are attributed to the ν_3 anti-symmetric stretching mode. The single band observed at 935 cm^{-1} is assigned to the ν_1 symmetric stretching mode. And two external modes were observed as 194 and 210 cm^{-1}. Both the site-group and Davydov (factor-group) splittings of PO_4 vibrations were observed in alforsite, which is similar to other phosphates such as chlorapatite (O'Shea et al. 1974), fluorapatite (Williams and Knittle 1996; Comodi et al. 2001a, b), $Pb_5(PO_4)_3Cl$ (Frost and Palmer 2007), tuite (Zhai et al. 2010), $Sr_3(PO_4)_2$ and $Ba_3(PO_4)_2$ (Zhai et al. 2011a), stronadelphite (Zhai et al. 2015a), whitlockite (Zhai et al. 2015b).

Pressure dependence of Raman spectra

High-pressure Raman spectra of $Ba_5(PO_4)_3Cl$ were collected up to 34.9 GPa and some Raman spectra were measured during decompression. Typical Raman spectra of $Ba_5(PO_4)_3Cl$ at high pressures are shown in Fig. 3. The quality of Raman spectra obtained during decompression is not as good. During compression and decompression some bands become unresolvable due to their weak intensity, especially for the external modes. It is obvious that, with increasing pressure, the Raman peaks of $Ba_5(PO_4)_3Cl$ gradually shift to higher frequencies. This is reasonable since the P–O and Ba–O bond lengths become shorter with increasing pressure and shorter bond lengths imply stronger bonds, i.e., larger force constant, and consequently higher vibrational frequency according to Hooke's law.

On the other hand, it is notable that a new Raman peak near the ν_2 symmetric bending modes appears at 20.5 GPa, and new bands near the ν_1 symmetric stretching and ν_4 anti-symmetric bending modes occur at 24.1 GPa, respectively. In this study Ar was used as pressure medium, and the pressure

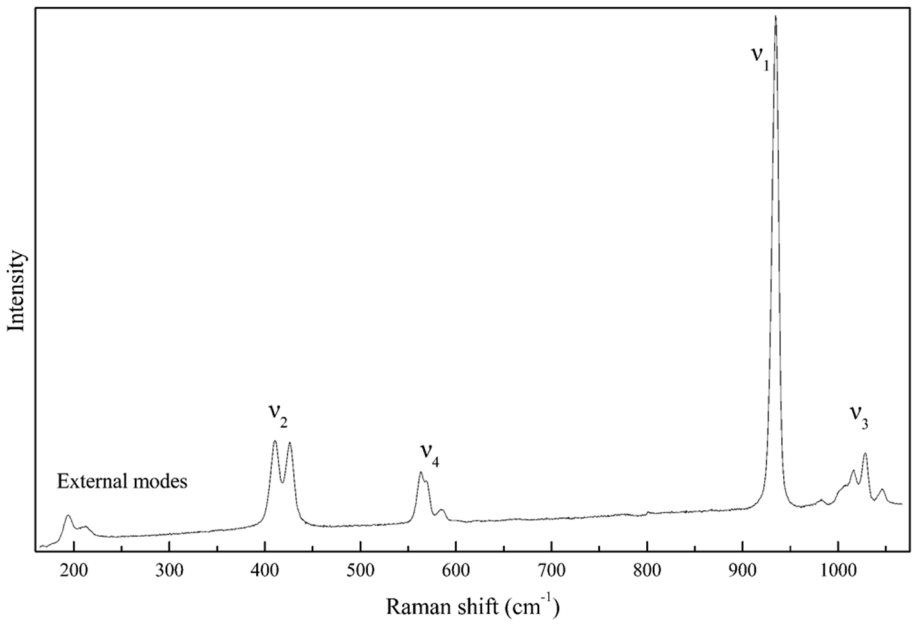

Fig. 2 Raman spectrum of $Ba_5(PO_4)_3Cl$ at ambient conditions

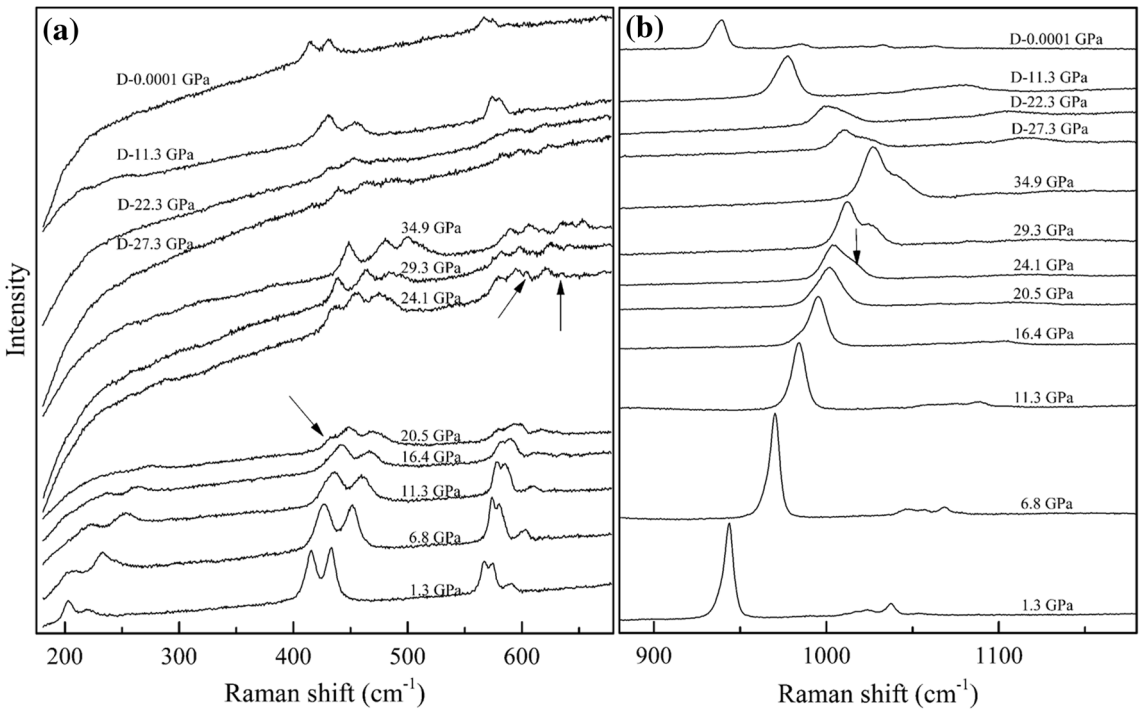

Fig. 3 Representative Raman spectra of $Ba_5(PO_4)_3Cl$ at high pressures and room temperature

gradients in the sample chamber increase more rapidly above ~20 GPa (Klotz et al. 2009) indicating a non-hydrostatic situation which may affect the Raman spectra. The new bands become more intense and remain up to the highest pressure in this study, but become weak during decompression and disappear after complete decompression to ambient pressure. These new bands might be regarded as new splittings of PO_4 internal modes under high pressures. In this case, the new splittings in $Ba_5(PO_4)_3Cl$ increase with pressure, as shown in Fig. 3, which indicates that the tetrahedral PO_4 distortion increases during compression. This observation is contrary to previous high-pressure Raman spectroscopic studies on $Ca_5(PO_4)_3F$ fluorapatite, which showed merging of the split bands, which indicated a decrease of tetrahedral PO_4 distortion during compression (Williams and Knittle 1996; Comodi et al. 2001a, b). The phenomenon is different from that of $Sr_5(PO_4)_3F$ stronadelphite, which showed new splitting of the ν_3 anti-symmetric stretching and ν_4 anti-symmetric bending vibrations during compression (Zhai et al. 2015a). This could result from the different local crystal field surrounding the PO_4 tetrahedra in $Ba_5(PO_4)_3Cl$, $Ca_5(PO_4)_3F$ and $Sr_5(PO_4)_3F$ under high pressures. However, currently there is no information about the evolution of PO_4 tetrahedra in the crystal structure of $Ba_5(PO_4)_3Cl$ and $Sr_5(PO_4)_3F$ during compression.

In a previous study, fluorapatite was investigated by in-situ single crystal X-ray diffraction and Raman spectral measurements to clarify the crystal evolution and vibrations of tetrahedral PO_4 at pressures up to 7 GPa (Comodi et al. 2001a, b). Their results showed a trend to standardization of PO_4 tetrahedra in fluorapatite since the tetrahedral quadratic elongation and tetrahedral angle variance decrease under high pressures, which causes the decreased splitting of PO_4 tetrahedra under high pressures. According to the method reported by Baur (1974), the distortion indices for PO_4 tetrahedra in alforsite, fluorapatite and stronadelphite at ambient conditions are calculated. The distortion indices of alforsite are identical with those of fluorapatite, but different from those of stronadelphite. The new splittings observed above 20 GPa may be caused by enhanced distortion of the PO_4 tetrahedra in $Ba_5(PO_4)_3Cl$, which needs to be confirmed by further high-pressure X-ray diffraction measurements.

Alternatively, the newly observed Raman bands in $Ba_5(PO_4)_3Cl$ above 20 GPa may be attributed to two crystallographically unique PO_4 tetrahedral sites that have different site distortions and site volumes. In this case the overall symmetry of the alforsite crystal structure could be lower, yielding the observed splitting. Further study is needed to clarify the evolution of PO_4 tetrahedra in alforsite under high pressures.

The Raman shift versus pressure plot of $Ba_5(PO_4)_3Cl$ is illustrated in Fig. 4. It is noted that, due to the relatively low intensities of the external vibrations and ν_3 anti-symmetric stretching mode of $Ba_5(PO_4)_3Cl$ at higher pressures, it is difficult to locate their peaks precisely. The quality of Raman spectra during decompression is not as good. Therefore, only

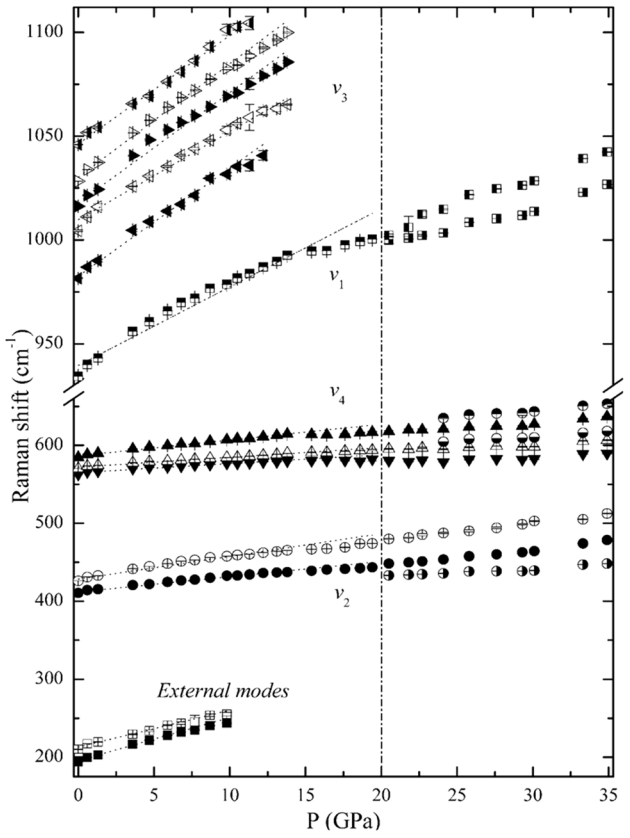

Fig. 4 Pressure dependence of the Raman bands of $Ba_5(PO_4)_3Cl$ at room temperature

available data for the external vibrations and ν_3 anti-symmetric stretching mode under high pressures during compression are shown in Fig. 4. The Raman shifts of active modes in $Ba_5(PO_4)_3Cl$ increase continuously with pressure, but the slopes vary with different modes.

As mentioned above, new Raman bands are observed above 20 GPa, may be attributed to enhanced distortion of the PO_4 tetrahedra during compression. On the other hand, the pressure gradients increase more rapidly above ~20 GPa (Klotz et al. 2009) since Ar was adopted as pressure medium. Therefore, the data points before the new splitting are quantitatively analyzed. As listed in Table 1, the pressure coefficients (β) of PO_4 internal modes in $Ba_5(PO_4)_3Cl$ alforsite indicate that ν_3 and ν_1 stretching modes in the high-frequency region are more sensitive to pressure compared to the ν_4 and ν_2 bending modes in the low-frequency region. The pressure coefficients of ν_3 and ν_1 modes in $Ba_5(PO_4)_3Cl$ alforsite are 4.24–5.46 and 3.77 cm^{-1}/GPa, whereas the pressure coefficients for ν_4 and ν_2 modes are 1.16–2.04 and 1.97–2.92 cm^{-1}/GPa, respectively. Meanwhile, the external modes show the largest pressure coefficients, which may be partially due to the more compressible barium polyhedra compared to PO_4 tetrahedra. The trends of pressure

Table 1 Parameters determined in the expressions of $\nu_P = \nu_{i0} + \beta P$ and $\gamma_{iT} = K_T(\partial \ln \nu_i / P)_T$ for $Ba_5(PO_4)_3Cl$ alforsite

	ν_0	ν_{i0}	β	R^2	γ_{iT}
PO_4 modes					
ν_3	1046	1046.3 (1)	5.22 (4)	0.992	0.357
	1028	1030.3 (3)	5.46 (1)	0.990	0.379
	1016	1017.9 (1)	5.31 (2)	0.987	0.374
	1004	1009.8 (2)	4.24 (3)	0.984	0.301
	982	982.6 (2)	5.20 (5)	0.991	0.379
ν_1	935	939.6 (1)	3.77 (1)	0.966	0.287
ν_4	585	586.4 (1)	2.04 (1)	0.965	0.249
	570	571.9 (1)	1.26 (1)	0.979	0.158
	563	564.9 (1)	1.16 (1)	0.960	0.147
ν_2	426	428.3 (1)	2.92 (1)	0.959	0.488
	411	411.8 (1)	1.97 (1)	0.971	0.343
External modes					
	210	213.1 (2)	4.71 (7)	0.962	1.583
	194	195.5 (1)	5.54 (2)	0.988	2.030

ν_P and ν_{i0} are in cm^{-1} and β is in cm^{-1} GPa^{-1}. ν_0 was observed frequency (in cm^{-1}) at ambient conditions. R^2 is the correlation coefficient. Grüneisen parameter γ_{iT} was calculated with isothermal bulk modulus of K_T=71.6 GPa estimated in this study

coefficients for different modes of $Ba_5(PO_4)_3Cl$ alforsite are similar to previous studies on $Ca_5(PO_4)_3F$, γ-$Ca_3(PO_4)_2$, $Sr_3(PO_4)_2$, $Ba_3(PO_4)_2$, β-$Ca_3(PO_4)_2$, and $Sr_5(PO_4)_3F$ (Williams and Knittle 1996; Comodi et al. 2001a; Zhai et al. 2010, 2011a, 2015a, b).

The pressure coefficients of the different Raman vibrations can be used to obtain the mode Grüneisen parameters, γ_{iT}, which can be determined from the following expression (Gillet et al. 1989):

$$\gamma_{iT} = K_T(\partial \ln \nu_i / \partial P)_T,$$

where ν_i is the vibrational frequency of the ith band and K_T is the isothermal bulk modulus. Though no experimental value for the isothermal bulk modulus for $Ba_5(PO_4)_3Cl$ alforsite has been reported, it can be estimated using the general relationship $K_0 \times V_0 =$ constant (Anderson and Anderson 1970) for a crystal structure. Based on the previous results of isothermal bulk moduli for synthetic and natural hexagonal apatites (Brunet et al. 1999; Comodi et al. 2001b; Matsukage et al. 2004), the isothermal bulk modulus for $Ba_5(PO_4)_3Cl$ is estimated as 71.6 GPa. Using this value, the γ_{iT} for different modes of $Ba_5(PO_4)_3Cl$ are calculated and shown in Table 1.

An average γ_{iT} value of 0.314 can be determined for the PO_4 modes in $Ba_5(PO_4)_3Cl$ alforsite, which is smaller to previous studies of PO_4 modes in some apatite-group minerals including fluorapatite (0.358, Williams and Knittle 1996; and 0.445; Comodi et al. 2001a) and stronadelphite $Sr_5(PO_4)_3F$ (0.332, Zhai et al. 2015a), and comparable to some other phosphate minerals including tuite (0.363,

Zhai et al. 2010), whitlockite (0.343, Zhai et al. 2015b), and $Sr_3(PO_4)_2$ (0.303, calculated using reported results of Zhai et al. [2011a, b]). The different average γ_{iT} value may partially indicate a different distortion and compressibility of the PO_4 tetrahedron in phosphates. Compared with the SiO_4 internal modes in some silicate minerals (Gillet et al. 1992, 1997), PO_4 internal modes in phosphate minerals show lower average isothermal mode Grüneisen parameters, which is reasonable since phosphates are more compressible than silicates.

The bulk thermochemical Grüneisen parameter, which is equal to $\alpha K_T V/C_v$ (where α is the thermal expansion, K_T is the bulk modulus, V is the molar volume and C_v is the volume constant heat capacity), can be estimated based on available parameters. Based on the results of Chernorukov et al. (2011), the thermal expansion coefficient α for alforsite is calculated as $3.62(9)\times10^{-5}$ K^{-1}, and the volume constant heat capacity C_v can be determined by the relationship between C_p and C_v ($C_p = C_v + a^2 K_T V T$), where C_p of $Ba_5(PO_4)_3Cl$ alforsite was reported as 383.5 J/mol K^{-1} in a previous study (Babu et al. 2011). Thus, the bulk thermochemical Grüneisen parameter is calculated as 1.44 for alforsite. Indeed a previous study has shown that the bulk Grüneisen parameters are usually in the range from 0.8 to 2 for incompressible oxide compounds without polymerized tetrahedra (Shankland and Bass 1988). It is known that the evolution of the PO_4 tetrahedral modes is not representative of the whole structural evolution of $Ba_5(PO_4)_3Cl$ alforsite. The external modes, including the vibrations associated with the barium polyhedra in alforsite, can strongly affect the bulk Grüneisen parameter. As listed in Table 1, the available Grüneisen parameters of the external modes are much larger than those of the PO_4 internal modes. Therefore, for alforsite and other phosphates, the relatively low average mode Grüneisen parameter of PO_4 tetrahedra indicates that the lattice modes are related to divalent cation substitutions that largely contribute to the bulk Grüneisen parameter.

Acknowledgements The manuscript was improved by Dr. Terry Mernagh. The authors thank Prof. T. Tsuchiya for his editorial handling. Critical comments and suggestion from two anonymous reviewers are helpful to improve the manuscript. This work was financially supported by National Natural Science Foundation of China (Grant no. 41372040), the Knowledge Innovation Program of the Institute of Geochemistry, Western Light Talents Training Program of Chinese Academy of Sciences, and by National Science and Engineering Research Council of Canada.

References

Allan DR, Angel RJ, Miletich R, Reichmann H, Brunet F (1996) High-pressure powder-diffraction studies of apatite $Ca_5(PO_4)_3(OH, F, Cl)$. ESRF report, experimental number:HC439

Anderson DL, Anderson OL (1970) The bulk modulus-volume relationship for oxides. J Geophys Res 75:3494–3500

Babu R, Jena H, Kutty KG, Nagarajan K (2011) Thermodynamic functions of $Ba_{10}(PO_4)_6Cl_2$, $Sr_{10}(PO_4)_6Cl_2$ and $Ca_{10}(PO_4)_6Cl_2$. Thermochim Acta 526:78–82

Baur WH (1974) The geometry of polyhedral distortions. Predictive relationships for the phosphate group. Acta Crystallogr B 30:1195–1215

Brunet F, Allan DR, Redfern SAT, Angel RJ, Miletich R, Reichmann HJ, Sergent J, Hanfland M (1999) Compressibility and thermal expansivity of synthetic apatites, $Ca_5(PO_4)_3X$ with X = OH, F and Cl. Eur J Miner 11:1023–1035

Chernorukov NG, Knyazev AV, Bulanov EN (2011) Phase transitions and thermal expansion of apatite-structured compounds. Inorg Mater 47:172–177

Comodi P, Liu Y, Frezzotti ML (2001a) Structural and vibrational behaviour of fluorapatite with pressure. Part II: in situ micro-Raman spectroscopic investigation. Phys Chem Miner 28:225–231

Comodi P, Liu Y, Zanazzi PF, Montagnoli M (2001b) Structural and vibrational behaviour of fluorapatite with pressure. Part I: in situ single-crystal X-ray diffraction investigation. Phys Chem Miner 28:219–224

Fan D, Ma M, Wei S, Chen Z, Xie H (2013a) In-situ synchrotron powder X-ray diffraction study of vanadinite at room temperature and high pressure. High Temp High Press 42:441–449

Fan D, Wei S, Liu J, Li Y, Xie H (2013b) X-ray diffraction study of calcium-lead fluorapatite solid solution at high pressure: the composition dependence of the bulk modulus and its pressure derivative. High Temp High Press 42:69–80

Fleet ME, Liu X, Shieh SR (2010) Structural change in lead fluorapatite at high pressure. Phys Chem Miner 37:1–9

Forien JB, Fleck C, Krywka C, Zolotoyabko E, Zaslansky P (2015) In situ compressibility of carbonated hydroxyapatite in tooth dentine measured under hydrostatic pressure by high energy X-ray diffraction. J Mech Behav Biomed Mater 50:171–179

Frost RL, Palmer SJ (2007) A Raman spectroscopic study of the phosphate mineral pyromorphite $Pb_5(PO_4)_3Cl$. Polyhedron 26:4533–4541

Gatta GD, Lee Y, Kao CC (2009) Elastic behavior of vanadinite, $Pb_{10}(VO_4)_6Cl_2$, a microporous non-zeolitic mineral. Phys Chem Miner 36:311–317

Gillet P, Guyot F, Malezieux JM (1989) High-pressure, high-temperature Raman spectroscopy of Ca_2GeO_4 (olivine form): some insights on anharmonicity. Phys Earth Planet Inter 58:141–154

Gillet P, Fiquet G, Maldzieux JM, Geiger C (1992) High-pressure and high-temperature Raman spectroscopy of end-member garnets: pyrope, grossular and andradite. Eur J Miner 4:651–664

Gillet P, Daniel I, Guyot F (1997) Anharmonic properties of Mg_2SiO_4-forsterite measured from the volume dependence of the Raman spectrum. Eur J Miner 9:255–262

Griffith WP (1969) Raman spectroscopy of minerals. Nature 224:264–266

Hata M, Marumo F, Iwai S (1979) Structure of barium chlorapatite. Acta Crystallogr B 35:2382–2384

He Q, Liu X, Hu X, Deng L, Chen Z, Li B, Fei Y (2012) Solid solutions between lead fluorapatite and lead fluorvanadate apatite: compressibility determined by using a diamond-anvil cell coupled with synchrotron X-ray diffraction. Phys Chem Miner 39:219–226

He Q, Liu X, Li B, Deng L, Chen Z, Liu X, Wang H (2013) Expansivity and compressibility of strontium fluorapatite and barium fluorapatite determined by in situ X-ray diffraction at high-T/P conditions: significance of the M-site cations. Phys Chem Miner 40:349–360

Hughes JM, Rakovan J (2002) The crystal structure of apatite, $Ca_5(PO_4)_3(F,OH,Cl)$. Rev Miner Geochem 48:1–12

Hughes JM, Rakovan JF (2015) Structurally robust, chemically diverse: apatite and apatite supergroup minerals. Elements 11:165–170

Huminicki DMC, Hawthorne FC (2002) The crystal chemistry of the phosphate minerals. Rev Miner Geochem 48:123–253

Ju G, Hu Y, Chen L, Wang X, Mu Z (2013) Persistent luminescence in $Ba_5(PO_4)_3Cl:Eu^{2+},R^{3+}$ (R = Y, La, Ce, Gd, Tb and Lu). Mater Res Bull 48:2598–2603

Kim D, Kim SC, Bae JS, Kim S, Kim SJ, Park JC (2016) Eu^{2+}-activated alkaline-earth halophosphates, $M_5(PO_4)_3X:Eu^{2+}$ (M = Ca, Sr, Ba; X = F, Cl, Br) for NUV-LEDs: Site-selective crystal field effect. Inorg Chem 55:8359–8370

Klee W (1970) The vibrational spectra of the phosphate ions in fluorapatite. Z Kristallogr 131:95–102

Klotz S, Chervin JC, Munsch P, Le Marchand G (2009) Hydrostatic limits of 11 pressure transmitting media. J Phys D: Appl Phys 42:075413

Liu X, Shieh SR, Fleet ME, Akhmetov A (2008) High-pressure study on lead fluorapatite. Am Miner 93:1581–1584

Liu X, Fleet ME, Shieh SR, He Q (2011a) Synthetic lead bromapatite: X-ray structure at ambient pressure and compressibility up to about 20 GPa. Phys Chem Miner 38:397–406

Liu X, Shieh SR, Fleet ME, Zhang L, He Q (2011b) Equation of state of carbonated hydroxylapatite at ambient temperature up to 10 GPa: Significance of carbonate. Am Miner 96:74–80

Mao HK, Bell PM, Shaner JW, Steinberg DJ (1978) Specific volume measurements of Cu, Mo, Pd and Ag and calibration of the ruby R_1 fluorescence pressure gauge from 0.06 to 1 Mbar. J Appl Phys 49:3276–3283

Matsukage KN, Ono S, Kawamoto T, Kikegawa T (2004) The compressibility of a natural apatite. Phys Chem Miner 31:580–584

Momma K, Izumi F (2011) VESTA 3 for three-dimensional visualization of crystal, volumetric and morphology data. J Appl Crystallogr 44:1272–1276

Newberry NG, Essene EJ, Peacor DR (1981) Alforsite, a new member of the apatite group: the barium analogue of chlorapatite. Am Miner 66:1050–1053

Noginov MA, Loutts GB, Bonner CE, Taylor S, Stefanos S, Wynne RM, Lasley BA (2000) Crystal growth and characterization of a new laser material, Nd: $Ba_5(PO_4)_3Cl$. J Opt Soc Am B 17:1329–1334

O'Reilly SY, Griffin WL (2000) Apatite in the mantle: implications for metasomatic processes and high heat production in Phanerozoic mantle. Lithos 53:217–232

O'Shea DC, Bartlett ML, Young RA (1974) Compositional analysis of apatites with laser-Raman spectroscopy: (OH, F, Cl) apatites. Arch Oral Biol 19:995–1006

Pan Y, Fleet ME (2002) Compositions of the apatite-group minerals: substitution mechanisms and controlling factors. Rev Miner Geochem 48:13–49

Pasero M, Kampf AR, Ferraris C, Pekov IV, Rakovan J, White TJ (2010) Nomenclature of the apatite supergroup minerals. Eur J Miner 22:163–179

Sato M, Tanaka T, Ohta M (1994) Photostimulated luminescence and structural characterization of $Ba_5(PO_4)_3Cl:Eu^{2+}$ phosphors. J Electrochem Soc 141:1851–1855

Shankland TJ, Bass JD (1988) Elastic properties and equations of state. American Geophysical Union, Washington, DC

Toumi M, Smiri-Dogguy L, Bulou A (2000) Crystal structure and polarized Raman spectra of $Ca_6Sm_2Na_2(PO_4)_6F_2$. J Solid State Chem 149:308–313

Wei S, Ma M, Fan D, Yang J, Zhou W, Li B, Chen Z, Xie H (2013) Compressibility of mimetite and pyromorphite at high pressure. High Pressure Res 33:27–34

White T, Ferraris C, Kim J, Madhavi S (2005) Apatite—an adaptive framework structure. Rev Miner Geochem 57:307–401

Williams Q, Knittle E (1996) Infrared and raman spectra of $Ca_5(PO_4)_3F$-flurapatite at high pressures: compression-induced changes in phosphate site and Davydov splitting. J Phys Chem Solid 57:417–422

Yoo HS, Vaidyanathan S, Kim SW, Jeon DY (2009) Synthesis and photoluminescence properties of Yb^{2+} doped $Ba_5(PO_4)_3Cl$ phosphor for white light-emitting diodes. Opt Mater 31:1555–1558

Yu XE, Hartl H, Schulz HJ, Thiede M (1988) Properties of barium chlorophosphate (apatite) luminophors activated by divalent europium. Z Anorg Allg Chem 567:60–68

Zhai S, Wu X, Ito E (2010) High-pressure Raman spectra of tuite, γ-$Ca_3(PO_4)_2$. J Raman Spectrosc 41:1011–1013

Zhai S, Liu A, Xue W, Song Y (2011a) High-pressure Raman spectroscopic studies on orthophosphates $Ba_3(PO_4)_2$ and $Sr_3(PO_4)_2$. Solid State Commun 151:276–279

Zhai S, Xue W, Yamazaki D, Shan S, Ito E, Tomioka N, Shimojuku A, Funakoshi K (2011b) Compressibility of strontium orthophosphate $Sr_3(PO_4)_2$ at high pressure. Phys Chem Miner 38:357–361

Zhai S, Shieh SR, Xue W, Xie T (2015a) Raman spectra of stronadelphite $Sr_5(PO_4)_3F$ at high pressures. Phys Chem Miner 42:579–585

Zhai S, Wu X, Xue W (2015b) Pressure-dependent Raman spectra of β-$Ca_3(PO_4)_2$ whitlockite. Phys Chem Miner 42:303–308